Siberian Arctic black carbon sources constrained by model and observation

Patrik Winiger[a], August Andersson[a], Sabine Eckhardt[b], Andreas Stohl[b], Igor P. Semiletov[c,d,e], Oleg V. Dudarev[d,e], Alexander Charkin[d,e], Natalia Shakhova[c,e], Zbigniew Klimont[f], Chris Heyes[f], and Örjan Gustafsson[a,1]

[a]Department of Environmental Science and Analytical Chemistry, The Bolin Centre for Climate Research, Stockholm University, 10691 Stockholm, Sweden; [b]Department of Atmospheric and Climate Research, Norwegian Institute for Air Research, N-2027 Kjeller, Norway; [c]International Arctic Research Center, University of Alaska Fairbanks, Fairbanks, AK 99775; [d]Pacific Oceanological Institute, Russian Academy of Sciences, 690041 Vladivostok, Russia; [e]Institute of Natural Resources, Geology and Mineral Exploration, Tomsk National Research Polytechnic University, 634034 Tomsk, Russia; and [f]Air Quality and Greenhouse Gases Program, International Institute for Applied Systems Analysis, 2361 Laxenburg, Austria

Edited by Mark H. Thiemens, University of California, San Diego, La Jolla, CA, and approved December 20, 2016 (received for review August 11, 2016)

Black carbon (BC) in haze and deposited on snow and ice can have strong effects on the radiative balance of the Arctic. There is a geographic bias in Arctic BC studies toward the Atlantic sector, with lack of observational constraints for the extensive Russian Siberian Arctic, spanning nearly half of the circum-Arctic. Here, 2 y of observations at Tiksi (East Siberian Arctic) establish a strong seasonality in both BC concentrations (8 ng·m^{-3} to 302 ng·m^{-3}) and dual-isotope–constrained sources (19 to 73% contribution from biomass burning). Comparisons between observations and a dispersion model, coupled to an anthropogenic emissions inventory and a fire emissions inventory, give mixed results. In the European Arctic, this model has proven to simulate BC concentrations and source contributions well. However, the model is less successful in reproducing BC concentrations and sources for the Russian Arctic. Using a Bayesian approach, we show that, in contrast to earlier studies, contributions from gas flaring (6%), power plants (9%), and open fires (12%) are relatively small, with the major sources instead being domestic (35%) and transport (38%). The observation-based evaluation of reported emissions identifies errors in spatial allocation of BC sources in the inventory and highlights the importance of improving emission distribution and source attribution, to develop reliable mitigation strategies for efficient reduction of BC impact on the Russian Arctic, one of the fastest-warming regions on Earth.

Arctic haze | atmospheric transport modeling | emission inventory | carbon isotopes | climate change

Black carbon (BC) is a short-lived climate pollutant, formed during incomplete combustion of biomass and fossil fuels and contributes to the amplified warming in the Arctic (1–4). However, estimates of the magnitude of added radiative forcing to the global atmosphere by BC span a large range (0.2 W·m^{-2} to 1 W·m^{-2}) (1, 5). Due to its short atmospheric lifetime, BC is a potential target for climate change mitigation. Historically, BC concentrations have been decreasing in the Arctic air (6), but their future fate is unclear. Projections range from increasing concentrations due to a decrease in rainfall (wet scavenging) (7), changes in wind patterns (8), an increase in emissions from wildfires (9), and increased shipping and extraction of natural resources (10) to decreasing concentrations due to more efficient wet scavenging (8). Chemical transport and climate model predictions of BC in the Arctic were, until recently, unsatisfactory and failed to reproduce the observed magnitude and amplitude of BC concentrations (11, 12). However, developments in atmospheric transport models show increasing model skills (12), especially for the European Arctic (13). A key component to the model–observation offset is the large uncertainty connected to emission inventories (EIs) (14–16) used by the models. Implications of these model uncertainties include challenges of accurately assessing the radiative forcing of BC (1, 17). Improvements in simulating BC concentrations have been shown to also improve simulation of aerosol optical depth (18). Several recent assessments urge for observation-based source apportionments to improve BC EIs (1, 19–23).

EIs are based on a bottom-up approach and heavily influenced by assumptions on emission factors (i.e., amount of BC released per amount of burned fuel in a given technology/source sector) and activity (i.e., amount of burnt fuel). Further, the spatially disaggregated national or regional inventories often use (coarse) large-scale proxies, such as total population, for aggregated sector categories (e.g., land transport, residential combustion), leading to spatial misallocation of sources. Even the most recent EI for Russia has an estimated range of total BC emissions that spans one order of magnitude (95% confidence) for anthropogenic emissions alone (24). This emphasizes the need for further source apportionment studies in this key source region for the Arctic, to eventually better understand climate effects of BC in the Arctic.

Carbon isotope characterization of elemental carbon (EC) aerosols [a BC analog (25)] has proven to be an important tool to constrain different BC source contributions (biomass burning vs. fossil fuel) and diagnose causes for differences between ^{14}C-based diagnostic source apportionment and EI models in different parts of the world (16, 26–31). Here, we present a 2-y study combining radiocarbon and stable carbon isotope analysis of EC in the vastly understudied Siberian Arctic (Tiksi). The total aerosol loading was collected continuously (16 April 2012 to 07 March 2014), with a high-volume sampler for total suspended particles (TSP), to meet the sample size requirements for natural abundance ^{14}C of the EC fraction. Many BC sources for Russia are reported as TSP by Russia's Federal State Statistics Service (24). These observations were directly compared with corresponding simulations with

Significance

A successful mitigation strategy for climate warming agents such as black carbon (BC) requires reliable source information from bottom-up emission inventory data, which can only be verified by observation. We measured BC in one of the fastest-warming and, at the same time, substantially understudied regions on our planet, the northeastern Siberian Arctic. Our observations, compared with an atmospheric transport model, imply that quantification and spatial allocation of emissions at high latitudes, specifically in the Russian Arctic, need improvement by reallocating emissions and significantly shifting source contributions for the transport, domestic, power plant, and gas flaring sectors. This strong shift in reported emissions has potentially considerable implications for climate modeling and BC mitigation efforts.

Author contributions: P.W., A.A., S.E., A.S., I.P.S., N.S., and Ö.G. designed research; P.W., A.A., S.E., O.V.D., A.C., N.S., Z.K., and C.H. performed research; P.W., A.A., S.E., A.S., I.P.S., Z.K., C.H., and Ö.G. analyzed data; and P.W., A.A., S.E., A.S., I.P.S., Z.K., and Ö.G. wrote the paper.

The authors declare no conflict of interest.

This article is a PNAS Direct Submission.

[1]To whom correspondence should be addressed. Email: Orjan.Gustafsson@aces.su.se.

This article contains supporting information online at www.pnas.org/lookup/suppl/doi:10.1073/pnas.1613401114/-/DCSupplemental.

the atmospheric transport model FLEXPART (flexible particle dispersion model) for the same site, coupled to the EI ECLIPSE (Evaluating the Climate and Air Quality Impacts of Short-Lived Pollutants) (23, 32), which was recently proven to emulate observations in the European Arctic well (13). The ECLIPSE EI can probably be considered the most suitable global EI for the Russian Arctic, because it also includes BC emissions from gas flaring, thought to be responsible for a significant portion of the Arctic BC burden (11, 24). Because ECLIPSE only covers anthropogenic emissions, open fire emissions (including agricultural waste burning and wildfires) were included by using the Global Fire Emissions Database (GFED), based on satellite data (33). The model results were then subject to forward isotope modeling to create a best-fit scenario for all modeled sources. This combination allowed for a direct comparison between top-down measurements and bottom-up simulations of BC concentrations and sources of biomass burning and fossil fuels, including biofuels, open fires, coal, liquid fossil fuels, and gas flaring.

Results

Meteorological Conditions. Tiksi (Fig. 1) displays the typical Arctic seasonal variability in meteorological conditions. The minimum and maximum temperatures during the campaign ranged from −48 °C to +19 °C (median −10 °C), with temperatures above freezing from June to September (34). Continental winds were usually prevalent (>50% of the time) during the cold months (October–May) (34), opening the gates for low-altitude transport of Eurasian pollution into the Arctic. In the warmer months (June–September), air masses were predominantly of marine

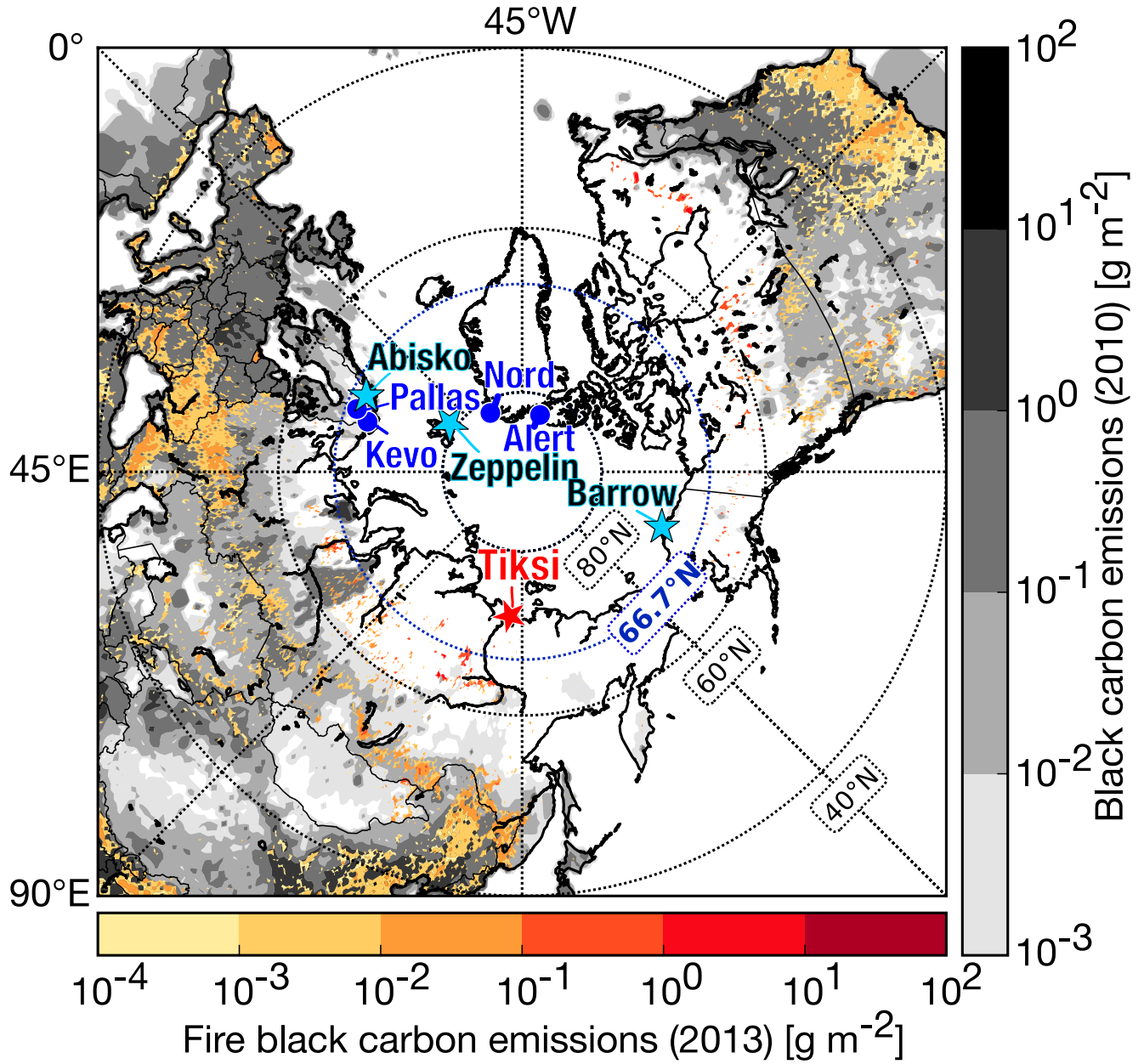

Fig. 1. Arctic observatories and BC emissions. The study site Tiksi (Russia) is shown as a red star, together with seven other major Arctic research sites. Stations for which BC radiocarbon data are available are marked with a star (Abisko, Barrow, Tiksi, and Zeppelin), and others are marked with a circle (Alert, Kevo, Nord, and Pallas). The map also shows the ECLIPSE bottom-up BC EI for the year 2010 (gray; log scale) and fire BC emissions of open fires from GFED (red; log scale) for the full year of 2013.

origin. Further general description of meteorological conditions during 2010–2014 can be found in Asmi et al. (34).

Temporally Varying Concentrations of Carbon Aerosols. Concentrations of EC (the mass-based analog of the optically defined BC) are typically elevated during the Arctic winter ("Arctic haze"). Not only are winter seasons dryer (less wet scavenging), but more efficient atmospheric transport of continental air into the Arctic along with a decrease of the boundary layer height lead to enhanced Arctic BC levels (35). Organic carbon (OC), on the other hand, tends to be elevated during the summer, owing to biomass burning (agricultural and wild fires), primary biogenic emissions (e.g., pollen), and secondary aerosol formation from biogenic volatile organic compounds (36). Observed concentrations of EC in Tiksi (Fig. 2) showed high seasonal variability (8 ng C·m^{-3} to 302 ng C·m^{-3}), with an overall average and SD of 47 ± 67 ng C·m^{-3} over the whole campaign and 35 ng C·m^{-3} to 57 ng C·m^{-3} over an uninterrupted full year, depending on the selected start and stop dates (Table S1). These levels were similar to observations of BC in Tiksi (12, 37) and comparable to other Arctic receptor sites in the European Arctic (38, 39). However, compared with the more frequently studied remote Arctic sites (Alert, Barrow, Station Nord, Summit, Pallas, and Zeppelin), Tiksi has higher BC concentrations.

Source-Diagnostic Isotopic Composition. Analysis of the dual-carbon signature of stable ($\delta^{13}C$) and radiocarbon ($\Delta^{14}C$) isotopes provides direct insight into the relative contribution of major BC emission source categories. The radiocarbon signature constrains the fraction of fossil fuel (devoid of ^{14}C) vs. contemporary biomass burning sources. The stable isotopic signature adds a dimension where sources can be further divided into biomass, coal, gas flaring, and liquid fossil fuel burning (28, 31). Furthermore, and specific to this study, liquid fossil fuels of Russian origin are considered, which carry a more depleted $\delta^{13}C$ signature, compared with the $\delta^{13}C$ signature found in "regular" liquid fossil fuels consumed in Western Europe or China (40) (Table S2). For the full 2-y study period, the concentration-weighted radiocarbon-based relative contribution (plus SD) of biomass burning to EC (f_{bb}) was 31 ± 19% with a large seasonal variability (Table S3), ranging from 19 ± 3% (or –762 ± 22‰ of $\Delta^{14}C$) in the winter to 73 ± 5% (or –105 ± 38‰ of $\Delta^{14}C$) in the summer (Fig. 2). The average for an uninterrupted full year (February 2013 to February 2014) demonstrated predominant influence by fossil sources with a fraction of biomass burning of 23 ± 19% to 32 ± 16%, again depending on the selection of the start and stop dates (Table S1).

Stable isotopes of EC spanned from –30.7 to –25.8‰, a range not uncommon for $\delta^{13}C$ of carbonaceous aerosols (31, 41). The $\delta^{13}C$ EC at Tiksi showed a similar seasonality to that of the radiocarbon-based fraction of biomass burning. Comparably enriched $\delta^{13}C$ signatures (≥–28.0‰) were observed during both summers, whereas, during the first winter, $\delta^{13}C$ was depleted (–30.7 to –29.0‰), and the second winter yielded values in the range of –28.2 to –26.9‰.

Model-Predicted vs. Observed Concentrations. Comparing the observations to model predictions makes it possible to draw conclusions on the quality of the underlying EI used for the computation, assuming the atmospheric transport model is accurate. Using this FLEXPART–ECLIPSE–GFED (FEG) model setup, produced simulations that matched quite accurately with the year-round observations of BC concentrations and source signatures in the European Arctic (13). For the full Tiksi campaign, the modeled average BC concentration of 39 ± 24 ng·m^{-3} (SD) matched the observational average of 47 ± 67 ng·m^{-3} (SD) (Table S1). However, the predictions of BC concentrations did not match the observed BC seasonality equally well for the East Siberian Arctic site (Fig. 2) as for the European Arctic site (13). For the Siberian Arctic site in the present study, there is an underprediction of BC concentration in the first summer (2012). A good match is observed during the consecutive fall and first half of the winter, with an underprediction of BC for the rest of the winter, even when one observed EC sample value of ~300 ng C·m^{-3} was disregarded (likely from local pollution from the town of Tiksi, ~10 km away). The FLEXPART footprint indicates strong local influence for that period (Fig. S1*F*). Analysis of the meteorological conditions also supports this interpretation (34). The low wind speeds and cold temperatures during that period suggest a shallow boundary layer, in which local pollution could accumulate. The BC concentration of the second fire season (summer/fall 2013) was strongly overpredicted. However, this low-BC concentration period is represented by only one long-term integrated sample/observation. The offset may also reflect an overestimation of open fires by GFED, or a close-by open fire included in GFED but not collected on the filter (33). Model predictions were again close to observed values in the subsequent fall and winter. The explanation for the overall observation–model mismatches is not a miscalculation of fire BC contributions alone; it is likely due to issues in the regional emissions in the global EI as well. Many local and regional sources near the receptor site appear to be misallocated or even missing, as has been reported before (12, 24). Additionally, the large-scale inventories appear not to be able to well represent the local source characteristics, such as potentially elevated BC emissions from gasoline vehicles in the winter (42, 43), local heating plants, and seasonal shipping. Given that the fall periods were among the best-predicted periods, it is worth noting that this period has been shown to be the most challenging in an earlier study of a European Arctic receptor site (13). Assuming that the transport model is accurate, we conclude that the discrepancies between model and observation root in (*i*) an incomplete anthropogenic EI, (*ii*) interpretation

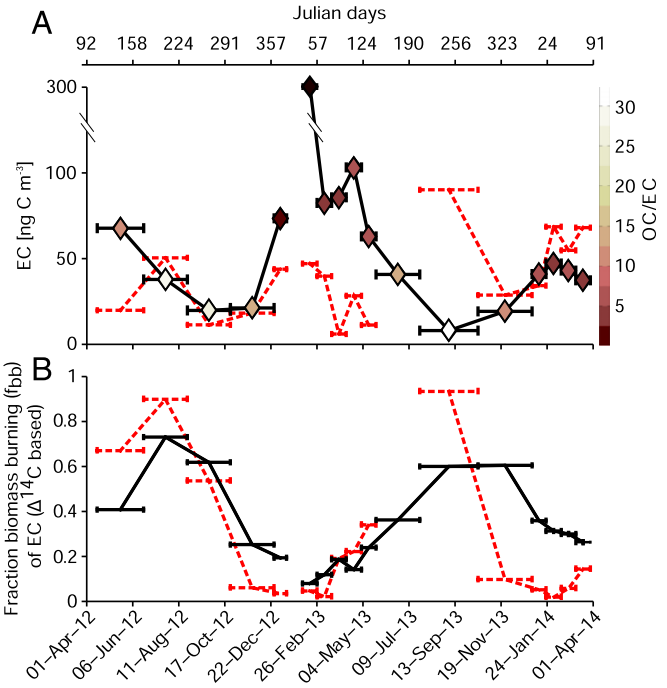

Fig. 2. Observation vs. prediction. Horizontal bars indicate sampling duration, and vertical error bars show observational uncertainties (SD). Dates are given as (*A*) Julian and (*B*) regular DD-MM-YY format. (*A*) EC concentration for top-down measured TSP (black line and diamond symbols) and bottom-up BC concentrations simulated with FLEXPART (dashed red line). The colorbar represents the OC/EC fraction for each TSP sample. (*B*) ^{14}C-based fraction of biomass burning (f_{bb}) for top-down measured TSP (black line and diamond symbols) and bottom-up BC (i.e., EC) simulated with FLEXPART (red line). The f_{bb} uncertainties for the TSP-based f_{bb} are shown but not visible (in general < 5% SD).

issues of the satellite data on which the fire emissions inventory is based, or (*iii*) potential model sampling errors due to spatial disaggregation—specifically, missing local sources.

Modeled vs. Observationally Constrained BC Source Contributions. The output from the FEG model can be divided into fossil (anthropogenic) and biomass (biofuels and natural) BC sources and thus directly be compared with the $^{13}C/^{14}C$-based observational source apportionment. Compared with the outcome of the concentration predictions, the model performed better when it came to simulating the BC sources (2-y model vs. observation has a linear R^2 of 0.51; $P < 0.01$). Due to the overprediction of biomass burning during both summers, followed by underpredictions during the second fall and both winters, the time-weighted average f_{bb} of 40 ± 32% (SD) is slightly higher than the observation value [30 ± 20% (SD); only observations/samples were included for which simulations were available]. The model-predicted seasonality was analogous to the observations but had higher amplitudes, with increased fractions of biomass burning during the summer and the opposite during winter months (Fig. 2). The predictions of the fire BC concentration in both summers lead to an estimated f_{bb} of 90% and 93% for 2012 and 2013, respectively (Table S1). Such high contributions of biomass burning to BC have only been observed before in the Arctic in the form of short and intense pollution events (31). Anthropogenic biofuels are, at all times, predicted by FEG to be no higher than 13%. In this regard, the ECLIPSE EI (32) is not much different from most recent estimates of Russian anthropogenic biofuels emission (24). The seasonality of anthropogenic emissions is, according to the Russian EI (24), the product of a wintertime relative increase in emissions of the Russian residential (consisting of 40% coal) and power plant sector (~100% coal), and the decrease of transportation and industry in the summer. The remaining major anthropogenic source in the EI (gas flaring) has little seasonality relative to other sources (24). Not taking into account potential source mixing during transport, the observational data (Fig. 3) appear to be dominated by liquid fossil fuels. The data are aligned on a trajectory toward the liquid fossil fuel $\delta^{13}C$ signature, with the higher EC concentrations closer to that end-member. However, no immediate conclusions can be drawn from this because the long sampling times could potentially skew observations of $\delta^{13}C$, causing invariably mixed isotopic fingerprints. Stohl et al. (11) predict that about 25% (annual mean) of the BC loading in the Tiksi region is from gas flaring, whereas the model predicts gas flaring BC contributions of 37% for the herein discussed simulations. However, the synchronous seasonality of predicted BC sources and f_{bb} based on $\Delta^{14}C$ appear to be quite accurate over the whole campaign.

Geographical Sources. FLEXPART transport modeling predicted that the majority of anthropogenic BC arriving to Tiksi was of Asian (mainly Russia, post-Soviet states, and China) origin (Fig. 3). European sources were contributing between 3% and 40%, and, on only one occasion, a partial North American origin (8%) was predicted. The fire contributions (excluding anthropogenic biofuels) ranged from 0 to 88%, in moderate agreement to the observed f_{bb} (linear $R^2 = 0.52$; $P < 0.02$).

The footprint emissions sensitivity shows that the majority of air masses had a Russian footprint (Fig. S1). The simulated BC source contribution showed two major distinct hot spots: (*i*) inside Russia and (*ii*) two greater-geographic regions on the Eurasian continent (Fig. S2). One of the hotspots was shared by the Nenets Autonomous Okrug and Komi Republic, both part of the Northwestern Federal District, whereas the second and bigger hotspot was located mostly in the two Autonomous Okrugs of Khanty-Mansi and Yamalo-Nenets, both part of the Ural Federal District. These two hotspots are the major oil and, especially, gas production sites in Russia, where virtually all of the Russian gas flaring BC emissions originate. However, the observed isotopic signatures of Tiksi BC in this current study suggest a smaller contribution from gas flaring, due to the relatively enriched $\delta^{13}C$ fingerprints of these samples. Currently, only one study on end-members of gas flaring exists (44), adding an unknown uncertainty to source estimates. The emissions of the two broader, geographic regions are most likely related to the relatively high population density accompanied by transport and, to some extent, power plant emissions. The geographic regions are, firstly, a pollution belt between 50°N and 60°N, spanning from 10°E to 110°E, and secondly, the North China Plain, with Beijing as economic centrum. Major emissions here are expected to be mainly coal, biofuels, and regular liquid fossil fuel. The predicted source contributions show that the major burden of BC arriving in the northeastern Siberian Arctic (Tiksi) originates from only a few source regions within Russia and China.

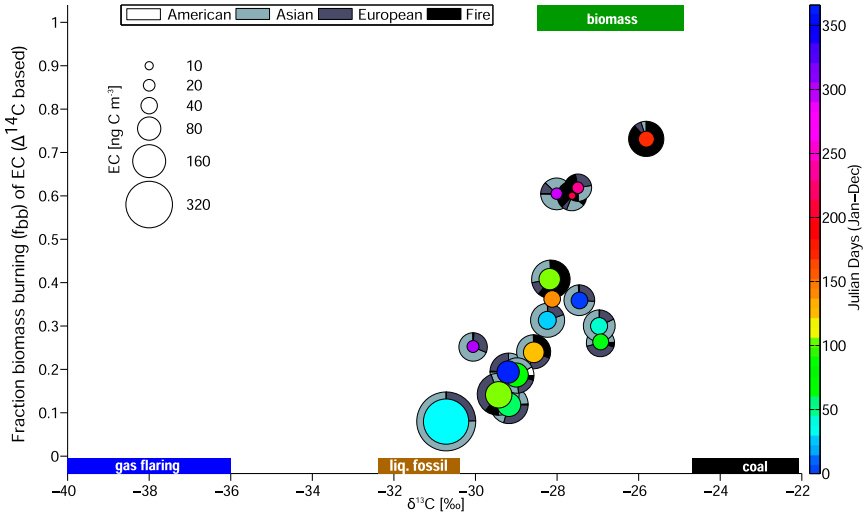

Fig. 3. Source apportionment in multiple dimensions. Shown is seasonal variation (color scale in Julian days) of observational isotope data. Size of the colored symbols indicates the EC concentration. Surrounding the colored symbols are rings in black and white, showing geographic sources influence, plus fire, obtained by FLEXPART. The expected $\delta^{13}C$ and $\Delta^{14}C$ end-member ranges for biomass burning emissions, gas flaring emissions, liquid fossil fuel combustion, and coal combustion are shown as green, blue, brown, and black bars, respectively (Table S2).

Bayesian Source Analysis. The FEG model showed that five major EI source classes influenced Tiksi: gas flaring, open fires (biomass burning), surface transport (i.e., liquid fossil), domestic, and power plants (i.e., coal). Emissions from the EI source classes waste and industry were below 2 ng C·m^{-3} at any given time and were therefore excluded from any further analysis. Domestic is a mixed source, composed of 60% biomass burning, 39% coal, and 1% liquid fossil (24). Given the δ^{13}C and Δ^{14}C end-member ranges (*SI Methods*, *Carbon Isotope End-Member Determination*) for these sources, the estimated carbon isotope signatures for each sample could be computed (forward modeling). The model-estimated dual carbon isotopes showed significant differences from observations in both carbon isotope dimensions (Fig. 4). However, it is not clear which source or which combination of sources caused this offset. To investigate the offset, a Bayesian statistical model was used, in which the FEG model estimated δ^{13}C and Δ^{14}C values were used as prior information. Each prior source estimate was associated with a conservative uncertainty of 16.3% (*SI Methods*, *Estimating the SD of the Priors*). The computation result is a posterior distribution of each source for each sample. The calculations were weighted by the influence of the sample duration for each sample. A Markov chain Monte Carlo (MCMC) approach (*SI Methods*, *MCMC Analysis*) was used to estimate the posterior distributions.

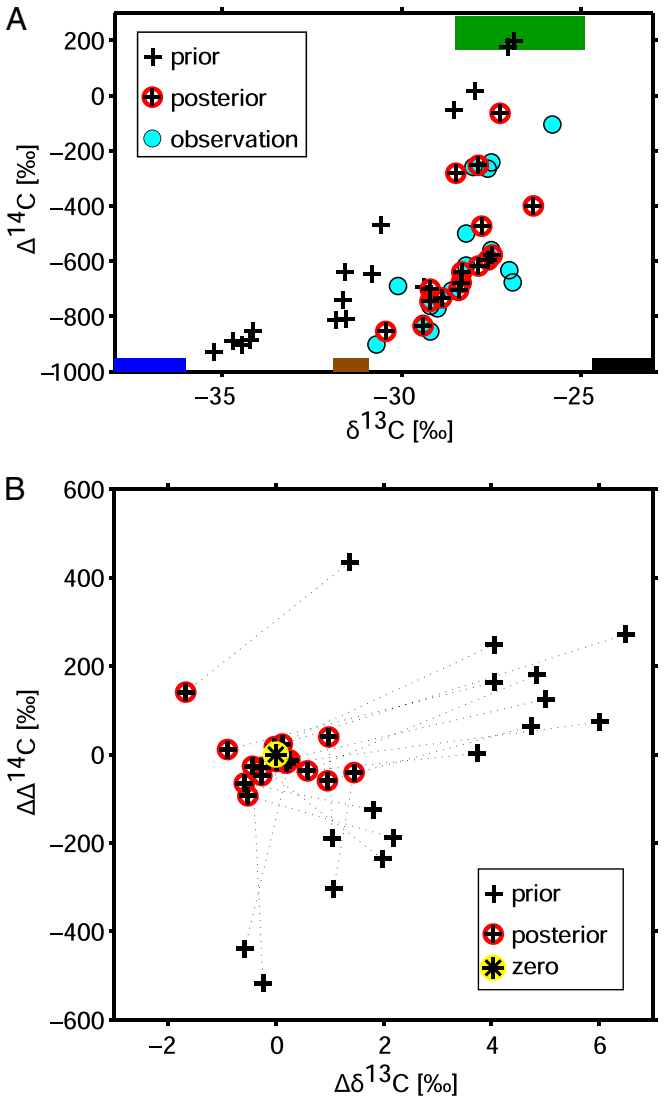

Fig. 4. Bayesian dual-isotope source contribution modeling. Prior model results (black cross) compared with its posterior (black cross inside red circle) (*A*) Model results (prior and posterior) compared with observations (blue filled circles). The expected δ^{13}C and Δ^{14}C end-member ranges for biomass burning emissions, gas flaring emissions, liquid fossil fuel combustion, and coal combustion are shown as green, blue, brown, and black bars, respectively (same as in Fig. 3). (*B*) Shift (Δ) of the modeled δ^{13}C and Δ^{14}C signatures of the prior (black cross) and posterior (black cross inside red circle) compared to the observations. The star in the yellow circle indicates the zero-shift point.

Using this uniformly applied but conservative prior, a modest but clear improvement is observed. However, this approach only allows for variations around the model means. In addition to such effects, there may also be systematic offsets that affect all sample data points. A best-fit scenario was investigated, comparing different models by shifting one or more of the BC sources, affecting all data points at the same time, rather than shifting each data point individually. By Bayesian model selection, using the Bayes factor (*SI Methods*, *Bayesian Model Comparison*), the general perturbation that gave the best fit was the combination of gas flaring and open fires. However, given the mass balance criterion, the perturbations of these two source classes affect the other three sources as well. Because the domestic source is mixed, this source was split into the relative contributions from the four "pure" emission fuels: liquid fossil, coal, gas flaring, and biomass burning, reflecting fuel types rather than combustion practices. Using this deconvolution, a much-improved posterior fit against the fraction of biomass burning based on observed Δ^{14}C data (Fig. 5) is obtained. The time-averaged observational fraction of biomass burning was 43.3%, the model prior gave 49.9%, and the posterior gave 42.5% (Fig. S3). The root-mean-squared deviation (RMSD) of the fraction of biomass burning prior against the observations was 26.3%, whereas the RMSD of the posterior against the observations was 5.1%, showing an improved fit for the posterior. The Bayesian analysis further suggested that the fractional contribution from coal increased (from 9 to 21%) relative to the prior, due to an increase of both the domestic and coal power sectors (Fig. 6). The fraction of liquid fossil fuel combustion increased overall (from 13 to 30%), and the gas flaring fraction decreased significantly (from 28 to 6%). The fossil sources showed some considerable variability, but less seasonality, especially coal and gas flaring, whereas liquid fossil contribution was more or less constant. Analyzing the five major EI source classes (Fig. 6), rather than the pure emission sources, further questions the bottom-up inventory data, pointing to the importance of independent evaluation of reported emissions. Much of the recent work focused on understanding Russian Arctic BC emissions and mitigation opportunities in transport sector (45, 46), whereas our analysis suggests that the domestic sector contribution might be of equal importance.

The discrepancies between the prior and posterior results may reflect multiple sources of uncertainties for the modeling, including bottom-up EIs, GFED parametrization, and the dispersion modeling. However, the forward modeling estimations of carbon isotope signatures from the priors are also affected by the representativeness of the end-member distributions, where the uncertainties are larger for the δ^{13}C dimension. The uncertainties for the observational carbon isotope analysis are expected to be well constrained within a limited range (absolute values of <50‰ for Δ^{14}C and <0.5‰ for δ^{13}C). Taken together, it is not exactly clear what caused the offset between observations and priors, but the posterior gives a much-improved view on the main emissions sources that affected Tiksi in the Siberian Arctic. Biomass burning appeared to be the most prevalent of all BC sources, followed by liquid fossil, coal, and, finally, gas flaring as least dominant source.

Discussion

Observations and model predictions of BC are disparate in the Russian Arctic and other high latitudes (12, 24, 47). At the same time, the Russian Arctic is one of the fastest-warming regions on our planet (48), especially in the spring season (high-temperature anomaly for March–April–May). The reasons for this

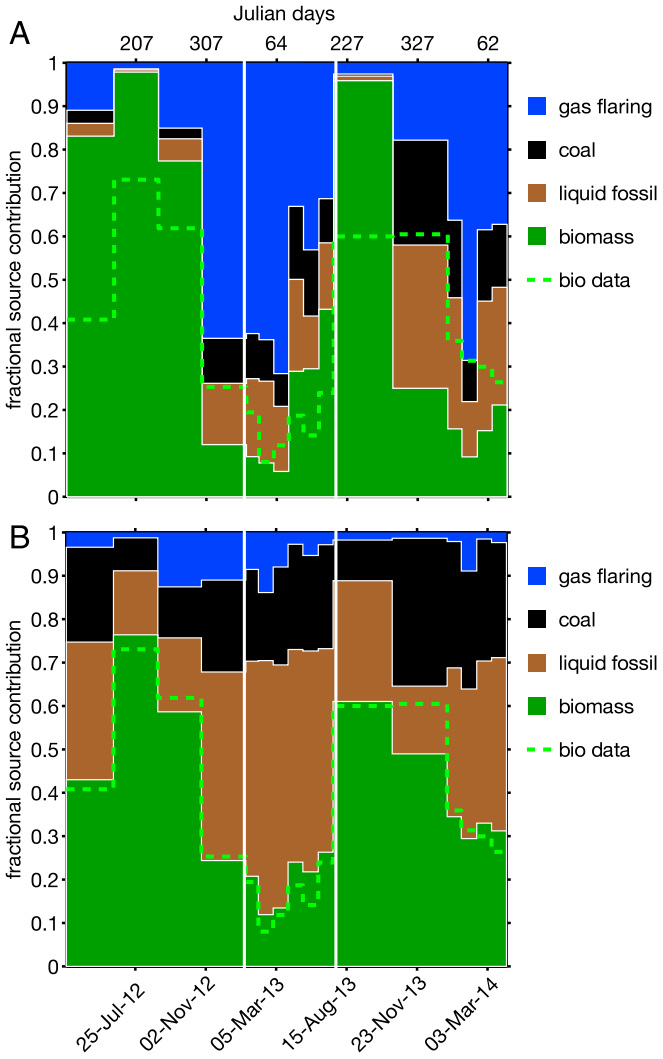

Fig. 5. Bayesian estimates of relative BC fuel type contributions. Dates are given as (*A*) Julian and (*B*) regular DD-MM-YY format. Computed fractional source contributions of the four BC-emission fuel-type sources, from top down: gas flaring emissions (blue), coal combustion (black), liquid fossil fuel combustion (brown), and biomass burning emissions (dark green). The dashed light green line shows the Δ^{14}C-based observed fraction biomass estimate. The two white vertical lines indicate interruptions in model/observation data (Table S1) (*A*) Model prior. (*B*) Model posterior (best fit).

anomaly are unclear. However, the BC burden for Tiksi is higher than for other remote sites, and it is especially high during the Arctic haze season in spring. Our 2-y observations showed clear and strong seasonality with respect to sources and concentrations of BC. The isotope-constrained source apportionment pinpointed that biomass burning was dominant during low BC concentration seasons in summer whereas fossil sources dominated the Arctic haze seasons. Although the FEG model overpredicted contributions of gas flaring and biomass burning to BC, the observed isotopic signature pointed to liquid fossil fuels and biomass burning as the major sources, or, in policy terms, the transport and domestic emission sectors. In this, and a previous independent isotope-based study of BC in the European Arctic (13), we found that gas flaring did not play a dominant role, contrary to expectations from current EIs. Both receptor sites (Abisko in Sweden and Tiksi in Russia) were at a similar, rather large, distance from the major gas flaring sources in the Northwestern and Ural Federals Districts, which could be one explanation of this finding. The applied model did not agree as well with observations in the northern Siberian Arctic as it did for the European Arctic. This was, in part, due to overestimation of biomass burning BC (fire emissions inventory) and underestimation of fossil fuel sources (anthropogenic EI). The latter is most likely caused by an inchoate EI, where entire regions and major sources, most likely of the liquid fossil fuel type, appear to be completely missing or significantly underestimated, e.g., road transport or shipping. The appearance of white spots in the EI and underestimation of observed BC in Tiksi could also be due to misallocation of sources, such as mining or nonroad transport, i.e., shipping on rivers, as well as transportation on frozen rivers. Smaller settlements could likely be misrepresented in the coarse spatial pattern of the inventory, and low local emissions could have a significant impact on observations. However, the overestimation of fossil (gas flaring) sources with occasional overestimation of biomass burning sources are the reason why predicted BC sources based on Δ^{14}C appear to be quite accurate, looking at the whole campaign.

Application of a Bayesian statistics-based model allowed creating a best-fit scenario (posterior) to the originally predicted

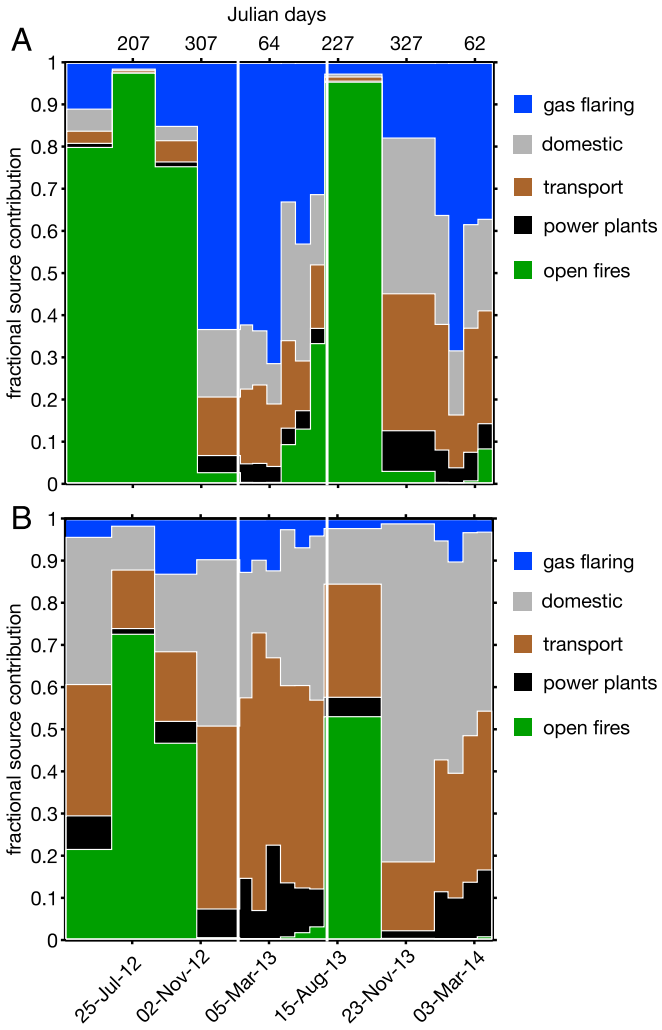

Fig. 6. Bayesian estimates of source sector contributions. Dates are given as (*A*) Julian and (*B*) regular DD-MM-YY format. Shown is computed fractional source contribution of the main four source sectors (within ECLIPSE) plus open fires (which includes wild fires as well as agricultural waste burning), from top down: gas flaring emissions (blue), domestic (gray), transport (brown), power plants (black), and open biomass burning emissions (dark green). The two white vertical lines indicate interruptions in model/observation data (Table S1) (*A*) Model prior. (*B*) Model posterior (best fit).

values by the model (prior). This posterior result underlined our previous observational findings. The contributions of gas flaring were overestimated, whereas contributions of liquid fossil (transport) and (domestic and power plant) coal were underestimated. The few exceptions of biomass burning overestimation can potentially be explained by positive fire count anomalies of local fire patches (33). Although the discrepancy of the gas flaring estimates and the observations could be due to issues within FLEXPART (e.g., too little wet scavenging causing a too-long BC lifetime and thus a too-large contribution of the remote flaring emissions relative to closer other sources), a too-long BC lifetime in the model would also lead to a general overestimation of observed BC, which is not the case. In addition, the gas flaring end-member could deviate from the herein applied value. This end-member depends on the hydrocarbon composition of the flared gas and, to a certain degree, on the biogeochemical origin of the hydrocarbons (49, 50), i.e., the isotope end-member is most likely dependent on the local origin of the gas flaring BC. Currently, only one study on the end-members of gas flaring exists (44), illustrating the need for more measurements, especially close to sources. Lastly, the model–observation dichotomy could be due to difference in actual 2012–2014 BC emissions versus the emission estimates used in this work, i.e., from the year 2010.

Conclusions

This continuous 2-y study provided an opportunity to compare observations and model predictions of BC in the vastly understudied northeastern Siberian Arctic. Our isotope-based observations showed that sources of pollution were, to a significant extent, due to liquid fossil fuel of Russian origin, identified by its distinct isotopic signature. A high seasonality was observed with regard to both BC concentrations and sources. Regardless of local pollution, the MCMC calculations showed that a best-fit model could be generated by reducing gas flaring (–84%) and open fire emissions (–53%) and increasing transport (+139%), domestic (+113%), and power plant (+109%) emissions. The emissions accounted for in the EI (which is coupled to the model) appear to be uncertain, and sources related to BC emissions received in northeastern Siberia seem to be poorly allocated in the inventory. Apparent misestimation of gas flaring and other sources could be due to the misallocation of distant or close sources, relative to the remote receptor site, or simply missing local sources. This uncertainty may also be higher due to, e.g., inaccurate scavenging coefficient and aerosol lifetime in the model, as well as unexpected end-member variations in the isotopic sources of gas flaring in the observation. BC concentrations at Tiksi are higher than at other remote sites in the Arctic, which suggests that local sources enhance the otherwise uniform Arctic background at Tiksi. However, there is a near-absence of BC emissions in northeastern Siberia in the EI inventory. This 2-y continuous record provides a robust baseline for assessing the current loadings, and for diagnosing areas for further improvement in modeling and observations—a necessity also for more reliable estimates of the climate effect of BC in the rapidly warming Russian Arctic.

Methods

The Far-East Siberian Arctic Receptor Site. The high-volume filtration systems were continuously operated for 24 mo in a specially constructed new sampling cabin at the observatory of the Russian Academy of Sciences (RAS), situated ∼10 km southwest of the Tiksi settlement to be away from immediate influence (Fig. S4). Tiksi is an urban settlement (population ∼2,000) situated on the Lena River Delta (34). The RAS Polar Geocosmophysical Observatory site (71.4°N, 128.5°E) was founded in 1958. Permanent technical staff attend the station on a daily basis. This study also benefitted from measurements of absorption-based BC measurements taken at the Tiksi Hydrometeorological Research Observatory, which opened in 2010, based on the 1932-founded Polyarka Station, 7 km south of the Tiksi settlement (34, 51).

EC and OC Analysis. Samples were collected from April 2012 to March 2014 with continuous sample intervals of 15 d to 25 d, depending on the weather conditions. The coldest winter temperatures turned out to be too demanding for the tubing used for the TSP inlet, which is why there is a 1-mo gap in observations (14 January 2013 to 6 February 2013), during which the tubing had to be replaced with a (low) temperature-resistant type. Aerosols were collected on precombusted quartz fiber filters (Millipore) using high-volume sampling with a TSP inlet (custom-built at Stockholm University). Carbonaceous aerosol concentrations (EC and OC) were measured with a standard thermal–optical transmission (TOT) analyzer (Sunset Laboratory Inc.) using the National Institute for Occupational Safety and Health 5040 method (52). Parts of the OC could potentially char during the application of this method. The OC would end up as pyrogenic carbon in the EC fraction, leading to an overestimation of the fraction of biomass burning. This potential effect has been evaluated in earlier work by sensitivity analysis, where it was found that the fraction of biomass burning could, in extreme cases, be overestimated by up to 7% (31). A total of 10 field blanks has been analyzed, all having EC concentrations below detection limit.

Carbon Isotope Analysis. The 33 samples were pooled into 17 composites, with emphasis on higher temporal resolution during the Arctic haze period. The isotopic analysis of EC was performed as described in previous work (13, 26, 31, 53). Briefly, the EC fraction was cryogenically trapped for further off-line isotopic analysis after regular Sunset TOT conversion to CO_2. Total sample size was at least 40 μg C. Both carbon isotopes were analyzed using accelerator mass spectrometry (AMS) at the United States National Science Foundation National Ocean Sciences Accelerator Mass Spectrometry Facility (53–55).

Fractions of biomass burning (which includes anthropogenic biofuels or wood combustion as well as natural wild fires) of EC were calculated based on the radiocarbon result (13), with an isotopic mass balance equation (26). Contemporary atmospheric CO_2 and freshly produced biomass have a $\Delta^{14}C$ end-member of ∼+25‰ (56). However, the most common source of biomass burning in the Arctic is wood, which has reported contemporary end-members between +90 and +282‰, depending on age and species (region) (56). Here, we apply a mean isotopic end-member for biomass BC of +225 ± 60‰, assuming a similar wood fuel turnover time and biota for the Eurasian boreal and northern temperate regions (31). The conservative variability of ±60‰ was restricted by MCMC simulation, leading to a mean variability (plus SD) in the fraction biomass burning of 3 ± 2%.

Open Fire Estimate by Satellite-Based Fire Emissions Inventory. The Global Fire Emissions Database, version GFED4.1s, was applied to get an estimate of the biomass burning contribution to BC (13). This fire emissions inventory is based on satellite data and quantifies open fires, as well as fires from agricultural waste burning (33, 57), as burned area product (Collection 5.1 Moderate Resolution Imaging Spectroradiometer) (33, 57, 58). The original resolution of 0.25 was changed to 0.5°. The monthly dataset includes small fires (59).

Transport Modeling with Bottom-Up Emission Inventory. To predict the BC concentrations at Tiksi, the particle dispersion model FLEXPART (60, 61), version 9.2, was applied in backward mode for the exact same time periods as the measurements (13). The simulations used meteorological operational analysis data from the European Centre for Medium-Range Weather Forecasts (ECMWF) at a resolution of 1°. One data point (in summer 2013) is missing due to ECMWF's increase of vertical model resolution on 25 June 2013. Simulations extended over 20 d back in time, sufficient to include most aerosol emissions arriving at the station, given a typical BC lifetime (∼1 wk). A mean particle diameter of 250 nm was used, with a logarithmic size distribution and a logarithmic SD (sigma) of 1.25. To estimate the anthropogenic BC emissions, FLEXPART was coupled to the ECLIPSE, version 5, EI based on the Greenhouse gas–Air pollution Interactions and Synergies model (62), using the year 2010 baseline scenario (23, 32). All emissions were available at yearly resolution for various source types, which were split into monthly resolution using monthly disaggregation factors from the ECLIPSE data set. Emissions from agricultural waste burning were excluded, because those were included in the GFED. Additionally, all emissions were explicitly split between biofuels (modern; e.g., wood burning) and fossil fuel emissions (Table S4).

Data Availability. The observational data that support the findings of this study are available on request from the corresponding author (Ö.G.) and will be available in the Bolin Centre Database (bolin.su.se/data/). EI data for GFED are freely available and can be found on the website www.globalfiredata.org/data.html. The FLEXPART model is freely available to the scientific community. It can be accessed under https://www.flexpart.eu/. For an ECLIPSE version with emissions split into fossil and biofuel, please contact Z.K. or C.H. directly. The data for total emissions of BC for different emission scenarios of ECLIPSE are freely available from IIASA: www.iiasa.ac.at/web/home/research/researchPrograms/air/Global_emissions.html.

ACKNOWLEDGMENTS. Eija Asmi and John Backman (Finnish Meteorological Institute) are acknowledged for numerous helpful discussions. We are also grateful to two anonymous reviewers for helpful comments on an earlier version of the manuscript. A.A., Ö.G., and P.W. acknowledge financial support from the Swedish Energy Agency (Contract 35450-2), the European Union under the 7th Framework Programme (FP7) [Compound Specific Isotopes (CSI):Environment, Contract PITN-GA-2010-264329], the Nordic Council of Ministries Defrost project as part of the Nordic Centre of Excellence, the Swedish Research Council Formas (Contract 942-2015-1070), and the European Research Council [ERC-Advanced Grant (AdG) Cryosphere-Carbon on Top of the Earth (CC-Top) Project 695331]. I.P.S. and A.C. acknowledge support from the Russian Government (Contract 14.Z50.31.0012/03.19.2014). N.S. and O.D. acknowledge the Russian Science Foundation (Contract 15-17-20032). ECMWF is acknowledged for meteorological data, and part of this study [Norwegian Institute for Air Research (NILU) and International Institute for Applied Systems Analysis (IIASA)] was funded under the FP7 ECLIPSE (Project 282688) and the Norwegian Research Council (NFR) project Emissions of Short-Lived Climate Forcers near and in the Arctic (SLICFONIA).

1. Bond TC, et al. (2013) Bounding the role of black carbon in the climate system: A scientific assessment. *J Geophys Res Atmos* 118(11):5380–5552.
2. Tedesco M, et al. (2016) The darkening of the Greenland ice sheet: Trends, drivers, and projections (1981–2100). *Cryosphere* 10(2):477–496.
3. Acosta Navarro JC, et al. (2016) Amplification of Arctic warming by past air pollution reductions in Europe. *Nat Geosci* 9(4):277–281.
4. Yang Q, Bitz CM, Doherty SJ (2014) Offsetting effects of aerosols on Arctic and global climate in the late 20th century. *Atmos Chem Phys* 14(8):3969–3975.
5. Myhre G, et al. (2013) Anthropogenic and natural radiative forcing. *Climate Change 2013: The Physical Science Basis. Contribution of Working Group I to the Fifth Assessment Report of the Intergovernmental Panel on Climate Change*, eds Stocker TF, et al. (Cambridge Univ Press, Cambridge, UK), pp 659–740.
6. Sharma S, et al. (2013) 16-year simulation of arctic black carbon: Transport, source contribution, and sensitivity analysis on deposition. *J Geophys Res Atmos* 118(2):943–964.
7. Allen RJ, Landuyt W, Rumbold ST (2015) An increase in aerosol burden and radiative effects in a warmer world. *Nat Clim Change* 6(3):269–274.
8. Jiao C, Flanner MG (2016) Changing black carbon transport to the Arctic from present day to the end of 21st century. *J Geophys Res Atmos* 121(9):4734–4750.
9. Veira A, Lasslop G, Kloster S (2016) Wildfires in a warmer climate: Emission fluxes, emission heights and black carbon concentrations in 2090–2099. *J Geophys Res Atmos* 121(7):3195–3223.
10. Barnhart KR, Miller CR, Overeem I, Kay JE (2015) Mapping the future expansion of Arctic open water. *Nat Clim Change* 6(3):280–285.
11. Stohl A, et al. (2013) Black carbon in the Arctic: The underestimated role of gas flaring and residential combustion emissions. *Atmos Chem Phys* 13(17):8833–8855.
12. Eckhardt S, et al. (2015) Current model capabilities for simulating black carbon and sulfate concentrations in the Arctic atmosphere: A multi-model evaluation using a comprehensive measurement data set. *Atmos Chem Phys* 15(16):9413–9433.
13. Winiger P, Andersson A, Eckhardt S, Stohl A, Gustafsson Ö (2016) The sources of atmospheric black carbon at a European gateway to the Arctic. *Nat Commun* 7:12776.
14. Bond TC, et al. (2004) A technology-based global inventory of black and organic carbon emissions from combustion. *J Geophys Res Atmos* 109(D14):D14203.
15. Zhao Y, Nielsen CP, Lei Y, McElroy MB, Hao J (2011) Quantifying the uncertainties of a bottom-up emission inventory of anthropogenic atmospheric pollutants in China. *Atmos Chem Phys* 11(5):2295–2308.
16. Chen B, et al. (2013) Source forensics of black carbon aerosols from China. *Environ Sci Technol* 47(16):9102–9108.
17. Gustafsson Ö, Ramanathan V (2016) Convergence on climate warming by black carbon aerosols. *Proc Natl Acad Sci USA* 113(16):4243–4245.
18. Wang H, et al. (2013) Sensitivity of remote aerosol distributions to representation of cloud–aerosol interactions in a global climate model. *Geosci Model Dev* 6(3):765–782.
19. Calvo Al, et al. (2013) Research on aerosol sources and chemical composition: Past, current and emerging issues. *Atmos Res* 120-121:1–28.
20. AMAP (2015) *AMAP Assessment 2015: Black Carbon and Ozone as Arctic Climate Forcers* (Arctic Monit Assess Program, Oslo).
21. Fuzzi S, et al. (2015) Particulate matter, air quality and climate: Lessons learned and future needs. *Atmos Chem Phys* 15(14):8217–8299.
22. Kodros JK, et al. (2015) Uncertainties in global aerosols and climate effects due to biofuel emissions. *Atmos Chem Phys* 15(15):8577–8596.
23. Stohl A, et al. (2015) Evaluating the climate and air quality impacts of short-lived pollutants. *Atmos Chem Phys* 15(18):10529–10566.
24. Huang K, et al. (2015) Russian anthropogenic black carbon: Emission reconstruction and Arctic black carbon simulation. *J Geophys Res Atmos* 120(21):11306–11333.
25. Petzold A, et al. (2013) Recommendations for reporting black carbon measurements. *Atmos Chem Phys* 13(16):8365–8379.
26. Gustafsson Ö, et al. (2009) Brown clouds over South Asia: Biomass or fossil fuel combustion? *Science* 323(5913):495–498.
27. Budhavant K, et al. (2015) Radiocarbon-based source apportionment of elemental carbon aerosols at two South Asian receptor observatories over a full annual cycle. *Environ Res Lett* 10(6):64004.
28. Andersson A, et al. (2015) Regionally-varying combustion sources of the January 2013 severe haze events over eastern China. *Environ Sci Technol* 49(4):2038–2043.
29. Zhang Y-L, et al. (2015) Fossil vs. non-fossil sources of fine carbonaceous aerosols in four Chinese cities during the extreme winter haze episode of 2013. *Atmos Chem Phys* 15(3):1299–1312.
30. Barrett TE, Robinson EM, Usenko S, Sheesley RJ (2015) Source contributions to wintertime elemental and organic carbon in the western Arctic based on radiocarbon and tracer apportionment. *Environ Sci Technol* 49(19):11631–11639.
31. Winiger P, Andersson A, Yttri KE, Tunved P, Gustafsson Ö (2015) Isotope-based source apportionment of EC aerosol particles during winter high-pollution events at the Zeppelin Observatory, Svalbard. *Environ Sci Technol* 49(19):11959–11966.
32. Klimont Z, et al. (October 20, 2016) Global anthropogenic emissions of particulate matter including black carbon. *Atmos Chem Phys Discuss*, 10.5194/acp-2016-880.
33. Giglio L, Randerson JT, van der Werf GR (2013) Analysis of daily, monthly, and annual burned area using the fourth-generation global fire emissions database (GFED4). *J Geophys Res Biogeosci* 118(1):317–328.
34. Asmi E, et al. (2016) Aerosol size distribution seasonal characteristics measured in Tiksi, Russian Arctic. *Atmos Chem Phys* 16(3):1271–1287.
35. Law KS, Stohl A (2007) Arctic air pollution: Origins and impacts. *Science* 315(5818): 1537–1540.
36. Tunved P, et al. (2006) High natural aerosol loading over boreal forests. *Science* 312(5771):261–263.
37. Fukasawa T, Ohta S, Murao N, Yamagata S, Makarov VN (1997) Aerosol observation in the Siberian Arctic. *Proc NIPR Symp Polar Meteorol Glaciol* 11:150–160.
38. Dutkiewicz VA, et al. (2014) Forty-seven years of weekly atmospheric black carbon measurements in the Finnish Arctic: Decrease in black carbon with declining emissions. *J Geophys Res Atmos* 119(12):7667–7683.
39. Hyvärinen AP, et al. (2011) Aerosol black carbon at five background measurement sites over Finland, a gateway to the Arctic. *Atmos Environ* 45(24):4042–4050.
40. Mašalaitė A, Garbaras A, Remeikis V (2012) Stable isotopes in environmental investigations. *Lith J Phys* 52(3):261–268.
41. Garbaras A, et al. (2015) Stable carbon fractionation in size-segregated aerosol particles produced by controlled biomass burning. *J Aerosol Sci* 79:86–96.
42. Mathis U, Mohr M, Forss A (2005) Comprehensive particle characterization of modern gasoline and diesel passenger cars at low ambient temperatures. *Atmos Environ* 39(1):107–117.
43. Nam E, et al. (2010) Temperature effects on particulate matter emissions from light-duty, gasoline-powered motor vehicles. *Environ Sci Technol* 44(12):4672–4677.
44. Widory D (2006) Combustibles, fuels and their combustion products: A view through carbon isotopes. *Combust Theory Model* 10(5):831–841.
45. US EPA (2016) *Black Carbon Diesel Initiative in the Russian Arctic*. Available at https://www.epa.gov/international-cooperation/black-carbon-diesel-initiative-russian-arctic. Accessed October 19, 2016.
46. Kholod N, Evans M, Kuklinski T (2016) Russia's black carbon emissions: Focus on diesel sources. *Atmos Chem Phys* 16(17):11267–11281.
47. Quinn PK, et al. (2008) Short-lived pollutants in the Arctic: Their climate impact and possible mitigation strategies. *Atmos Chem Phys* 8(7):1723–1735.
48. Hansen J, Ruedy R, Sato M, Lo K (2010) Global surface temperature change. *Rev Geophys* 48(4):RG4004.
49. Fjellanger E, et al. (2010) Charging the giant gas fields of the NW Siberia basin. *Petroleum Geology: From Mature Basins to New Frontiers—Proceedings of the 7th Petroleum Geology Conference* (Geol Soc London, London), pp 659–668.
50. Fuex A (1977) The use of stable carbon isotopes in hydrocarbon exploration. *J Geochem Explor* 7:155–188.
51. Uttal T, Makshats A, Laurila T (2013) The Tiksi International Hydrometeorological Observatory. *WMO Bull* 62(1):22–26.
52. Birch ME, Cary RA (1996) Elemental carbon-based method for monitoring occupational exposures to particulate diesel exhaust. *Aerosol Sci Technol* 25(3):221–241.
53. Zencak Z, Elmquist M, Gustafsson Ö (2007) Quantification and radiocarbon source apportionment of black carbon in atmospheric aerosols using the CTO-375 method. *Atmos Environ* 41(36):7895–7906.
54. McNichol AP, Gagnon AR, Jones GA, Osborne EA (1992) Illumination of a black box: Analysis of gas composition during graphite target preparation. *Radiocarbon* 34(3):321–329.
55. Pearson A, Mcnichol AP, Schneider RJ, von Reden KF, Zheng Y (1998) Microscale AMS 14C measurement at NOSAMS. *Radiocarbon* 40(1):61–75.
56. Mouteva GO, et al. (2015) Black carbon aerosol dynamics and isotopic composition in Alaska linked with boreal fire emissions and depth of burn in organic soils. *Global Biogeochem Cycles* 29(11):1977–2000.
57. van der Werf GR, et al. (2010) Global fire emissions and the contribution of deforestation, savanna, forest, agricultural, and peat fires (1997–2009). *Atmos Chem Phys* 10(23):11707–11735.
58. Giglio L, Loboda T, Roy DP, Quayle B, Justice CO (2009) An active-fire based burned area mapping algorithm for the MODIS sensor. *Remote Sens Environ* 113(2):408–420.
59. Randerson JT, Chen Y, van der Werf GR, Rogers BM, Morton DC (2012) Global burned area and biomass burning emissions from small fires. *J Geophys Res Biogeosci* 117(G4):G04012.
60. Stohl A, Forster C, Frank A, Seibert P, Wotawa G (2005) Technical note: The Lagrangian particle dispersion model FLEXPART version 6.2. *Atmos Chem Phys* 5(9): 2461–2474.
61. Stohl A, Hittenberger M, Wotawa G (1998) Validation of the Lagrangian particle dispersion model FLEXPART against large-scale tracer experiment data. *Atmos Environ* 32(24):4245–4264.
62. Amann M, et al. (2011) Cost-effective control of air quality and greenhouse gases in Europe: Modeling and policy applications. *Environ Model Softw* 26(12):1489–1501.
63. Hastings WK (1970) Monte Carlo sampling methods using Markov chains and their applications. *Biometrika* 57(1):97–109.
64. Metropolis N, Rosenbluth AW, Rosenbluth MN, Teller AH, Teller E (1953) Equation of state calculations by fast computing machines. *J Chem Phys* 21(6):1087–1092.

Supporting Information

Winiger et al. 10.1073/pnas.1613401114

SI Methods

Carbon Isotope End-Member Determination. The end-member values (source-specific signatures) of the carbon isotopes were compiled from the literature (Table S2). The fossil $\Delta^{14}C$ sources (liquid fossil, coal, and gas flaring) are well constrained at −1,000 ± 0‰. The main source of biomass in Russia is wood burning, estimated at +225 ± 60‰ (13, 31). The $\delta^{13}C$ end-member values for coal (−23.4 ± 1.3‰) and biomass (C3 plants, −26.7 ± 1.8‰) were collected from the literature review conducted by Andersson et al. (28). The liquid fossil end-member was taken from typical liquid fossil sources used in Russia (−31.4 ± 1‰) (40). The perhaps most uncertain end-member is the $\delta^{13}C$ value for gas flaring. Here a wide variability of 3‰ is used, but the average position may be dependent on the relative contribution from the different gas components, e.g., methane, ethane, and propane, which all have quite varying $\delta^{13}C$-value signatures, although methane is expected to dominate the mixtures ($\delta^{13}C$ for methane ≈ –60‰). Notable is that BC formation, in general, is associated with an enrichment in the $\delta^{13}C$ isotope (higher $\delta^{13}C$), because the lighter ^{12}C is more prone to CO_2 formation. However, an enrichment of more than a few per mill is not expected. In general, $\delta^{13}C$ lower than –38‰ is expected for certain situations (corresponding to an even lower posterior flaring contribution). Here, –38‰ was used in agreement with the (to our knowledge) only published $\delta^{13}C$ characterization of BC from gas flaring (44).

Domestic is a mixed source (60% biomass, 39% coal, and 1% liquid fossil) (24). The end-member values (for both $\delta^{13}C$ and $\Delta^{14}C$) were estimated assuming normal distribution mixing, where the mean (μ) and SD (σ) were estimated as:

$$\mu_D = 0.6 \times \mu_B + 0.39 \times \mu_C + 0.01 \times \mu_L \quad \text{[S1a]}$$

$$\sigma_D = \sqrt{(0.6 \times \sigma_B)^2 + (0.39 \times \sigma_C)^2 + (0.01 \times \sigma_L)^2}, \quad \text{[S1b]}$$

where D = domestic, B = biomass, C = coal, and L = liquid fossil.

Estimating the SD of the Priors. The fractional source contribution priors for the Bayesian analysis are assumed to be normally distributed with a mean (μ) equal to the FEG model results. The second parameter in the normal distribution is the SD (σ), which also needs to be estimated. BC bottom-up EIs typically report large uncertainties (e.g., 125 to 500%) in the flux (14, 15). However, the uncertainties for the fractional contributions from different sources need to be lower (<100%), as constrained by the mass balance criterion. To fully estimate the uncertainties of the relative source contributions to Tiksi BC levels from the FEG model would mean a vast modeling effort, i.e., coupled uncertainty propagation from FLEXPART, ECLIPSE, and GFED. Instead, given the comparably large expected uncertainties of the FEG modeling results, we estimated the uncertainties (σ) using the weakest assumptions of prior knowledge: Each possible fractional source combination is equally probable. The distribution that describes this scenario for n sources (here $n = 5$) is the n-dimensional Dirichlet distribution where the shape factors (α) are all equal to 1 (a.k.a., the n-dimensional standard simplex). The SD of the marginal distribution (the distribution of one of the fractional source contributions) of this symmetric Dirichlet distribution is given by:

$$\sigma = \sqrt{\frac{n-1}{n^2 \times (n+1)}}. \quad \text{[S2]}$$

Five sources thus give an uncertainty of roughly 16.3%. For comparison, the two-source case of this Dirichlet distribution is the standard uniform distribution, with $\sigma \approx 28.9\%$.

MCMC Analysis. The MCMC analysis was conducted using in-house scripts written in Matlab (ver. 2014b). A Metropolis–Hastings algorithm (63, 64) was used for sampling the parameter space, using 1,000,000 iterations, a burn-in of 10,000, and a data thinning of 10. The jump size of the stochastic perturbation was adjusted to obtain an acceptance rate of ∼0.23. The end-member distributions were described with normal distributions (28). The different samples were given different weight in the fitting, depending on observational sampling duration. The prior relative source distributions before the Bayesian modeling were assigned with normal distributions with (mean) values from the FEG model, and with an SD of 16.3%. For the sources where a general shift was introduced, the prior was exchanged from one per sample to one parameter affecting all samples, where the shift (here exemplified by gas flaring, x_F) was allowed to take any positive number, exemplified as:

$$f_F(j)_{posterior} = \frac{x_F \times f_F(j)_{prior}}{x_F \times f_F(j)_{prior} + f_{OF}(j)_{prior} + f_C(j)_{prior} + f_L(j)_{prior} + f_D(j)_{prior}} \quad \text{[S3a]}$$

$$f_{OF}(j)_{posterior} = \frac{f_{OF}(j)_{prior}}{x_F \times f_F(j)_{prior} + f_{OF}(j)_{prior} + f_C(j)_{prior} + f_L(j)_{prior} + f_D(j)_{prior}} \quad \text{[S3b]}$$

$$f_C(j)_{posterior} = \frac{f_C(j)_{prior}}{x_F \times f_F(j)_{prior} + f_{OF}(j)_{prior} + f_C(j)_{prior} + f_L(j)_{prior} + f_D(j)_{prior}} \quad \text{[S3c]}$$

$$f_L(j)_{posterior} = \frac{f_L(j)_{prior}}{x_F \times f_F(j)_{prior} + f_{OF}(j)_{prior} + f_C(j)_{prior} + f_L(j)_{prior} + f_D(j)_{prior}} \quad \text{[S3d]}$$

$$f_D(j)_{posterior} = \frac{f_D(j)_{prior}}{x_F \times f_F(j)_{prior} + f_{OF}(j)_{prior} + f_C(j)_{prior} + f_L(j)_{prior} + f_D(j)_{prior}}, \quad \text{[S3e]}$$

where F = gas flaring, OF = open fires, C = coal, L = liquid fossil, D = domestic, and f denotes the corresponding fractional contributions. The index j denotes sample number. Thus, if x takes on a value larger than 1, the overall fractional contribution of source gas flaring increases (and all others

decrease), and, if it is smaller than 1, it decreases (and all others increase).

Bayesian Model Comparison. For comparing the significance of the data fit for different models, evaluation of the Bayes factor is a powerful approach. In the present case, the different models that were compared shifted the importance of one or more sources to better fit with the observational data, i.e., the $\Delta^{14}C$ and $\delta^{13}C$ data for EC. The Bayes factor (K) is defined as the conditional probability (P) of data (D) given model 1 (the evidence for model 1, M_1) divided by the conditional probability for data given model 2 (the evidence for model 2, M_2):

$$K = \frac{P(D|M_1)}{P(D|M_2)}. \quad \textbf{[S4]}$$

The evidence for a model was computed by integrating (marginalizing) over the parameters assigned to that model. As an example, the Bayes factor comparing shifting both flaring (F) and open fires (OF) vs. shifting only flaring is given by the ratio between the evidence for the first model divided by the evidence for the second:

$$K = \frac{\iint P(D|x_F, x_{OF},\ M_{F,OF}) \times P(x_F, x_{OF}|M_{F,OF})dx_F dx_{OF}}{\int P(D|x_F,\ M_F) \times P(x_F|M_F)dx_F}, \quad \textbf{[S5]}$$

where x denotes the shifting factor. For the present example, two shifting factors are associated with model 1 and one shifting factor for model 2. The evidence for each model was computed separately (within model approach) using MCMC sampling over the parameter space, and the Bayes factor was computed through combinatorial comparison of the different models. For this particular case (comparing the two models with the best fits), the Bayes factor is >100, which is a "decisive" or "very strong" in favor of the combination of combining gas flaring and open fires. Adding a third parameter, e.g., coal, does not significantly improve the fit, as the Bayes factor is ~1. An advantage with using Bayes factors for model comparisons is that the degrees of freedom, e.g., the number of sources that are shifted, are naturally incorporated in the integral in Eq. **S5**.

Winiger et al. www.pnas.org/cgi/content/short/1613401114

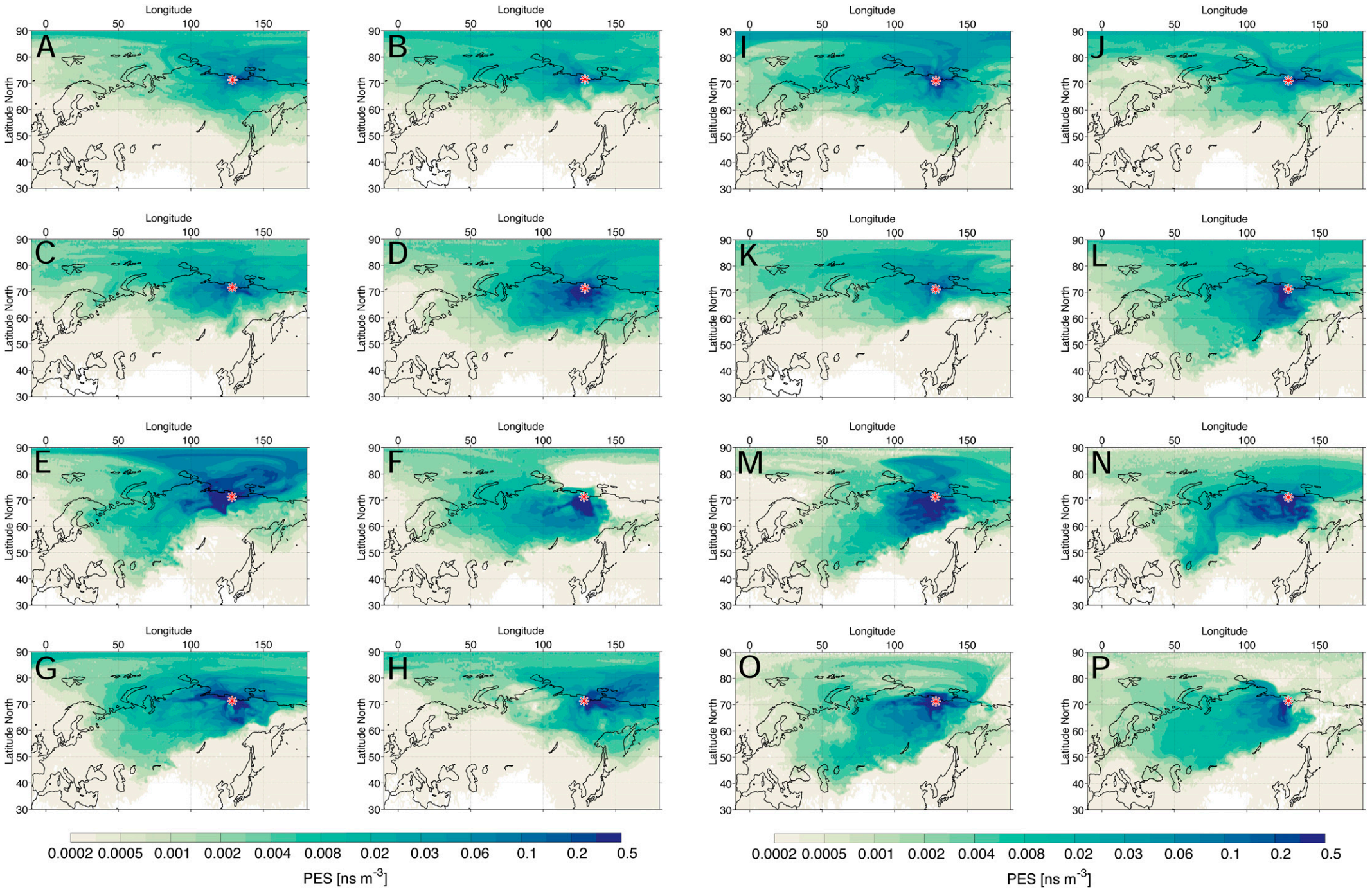

Fig. S1. FLEXPART footprints. FLEXPART potential footprint emission sensitivity (PES) for the BC aerosol tracer arriving at Tiksi, Russia (red star). (*A*) Isotope data point (given as range with yyyy-mm-dd) 2012-04-16 to 2012-06-21. (*B*) Isotope data point 2012-06-21 to 2012-08-24. (*C*) Isotope data point 2012-08-24 to 2012-10-25. (*D*) Isotope data point 2012-10-25 to 2012-12-27. (*E*) Isotope data point 2012-12-27 to 2013-01-14. (*F*) Isotope data point 2013-02-06 to 2013-02-27. (*G*) Isotope data point 2013-02-27 to 2013-03-20. (*H*) Isotope data point 2013-03-20 to 2013-04-10. (*I*) Isotope data point 2013-04-10 to 2013-05-02. (*J*) Isotope data point 2013-05-02 to 2013-05-23. (*K*) Isotope data point 2013-07-25 to 2013-10-17. (*L*) Isotope data point 2013-10-17 to 2014-01-02. (*M*) Isotope data point 2014-01-02 to 2014-01-23. (*N*) Isotope data point 2014-01-23 to 2014-02-14. (*O*) Isotope data point 2014-02-14 to 2014-03-07. (*P*) Isotope data point 2014-03-07 to 2014-03-28.

Winiger et al. www.pnas.org/cgi/content/short/1613401114

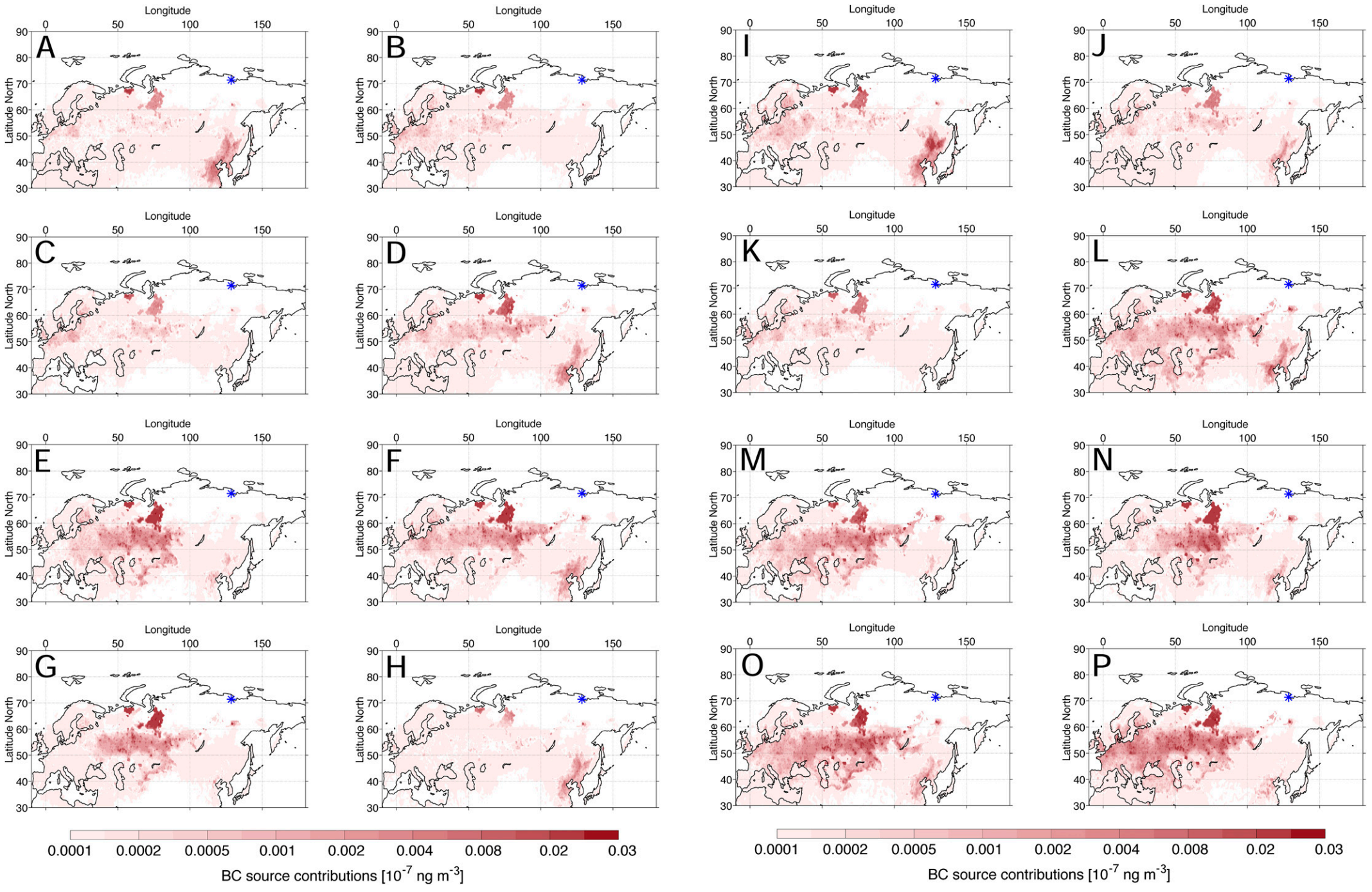

Fig. S2. FLEXPART BC source contributions. FLEXPART geographical distribution of the anthropogenic BC source contribution to the simulated mixing ratio at Tiksi, Russia (blue star). (*A*) Isotope data point (given as range with yyyy-mm-dd) 2012-04-16 to 2012-06-21. (*B*) Isotope data point 2012-06-21 to 2012-08-24. (*C*) Isotope data point 2012-08-24 to 2012-10-25. (*D*) Isotope data point 2012-10-25 to 2012-12-27. (*E*) Isotope data point 2012-12-27 to 2013-01-14. (*F*) Isotope data point 2013-02-06 to 2013-02-27. (*G*) Isotope data point 2013-02-27 to 2013-03-20. (*H*) Isotope data point 2013-03-20 to 2013-04-10. (*I*) Isotope data point 2013-04-10 to 2013-05-02. (*J*) Isotope data point 2013-05-02 to 2013-05-23. (*K*) Isotope data point 2013-07-25 to 2013-10-17. (*L*) Isotope data point 2013-10-17 to 2014-01-02. (*M*) Isotope data point 2014-01-02 to 2014-01-23. (*N*) Isotope data point 2014-01-23 to 2014-02-14. (*O*) Isotope data point 2014-02-14 to 2014-03-07. (*P*) Isotope data point 2014-03-07 to 2014-03-28.

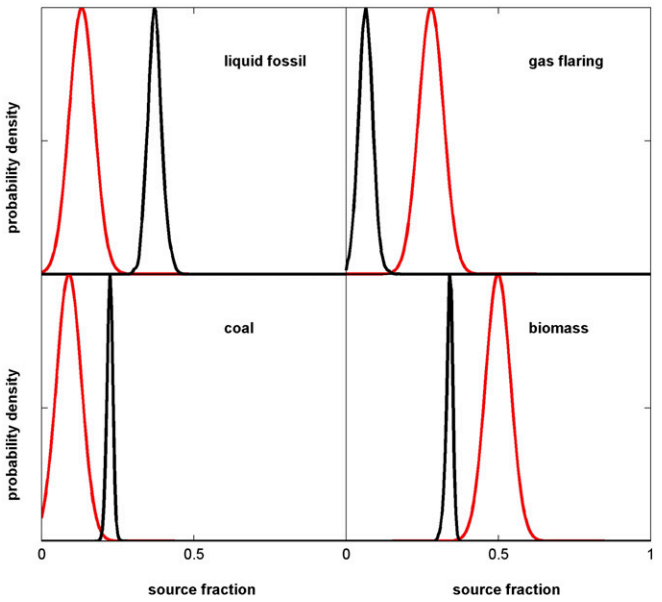

Fig. S3. Mean Bayesian source contributions. Prior (red) and posterior (black) mean fractions of the four fuel-type emissions sources from the Bayesian modeling for the full campaign (2 y). Note that the SD for the prior in these plots is not 16.3%, as they are the average of the 16 data points. Instead, it is calculated as 16.3 divided by $16^{0.5}$ (~4%), reflecting the temporal averaging.

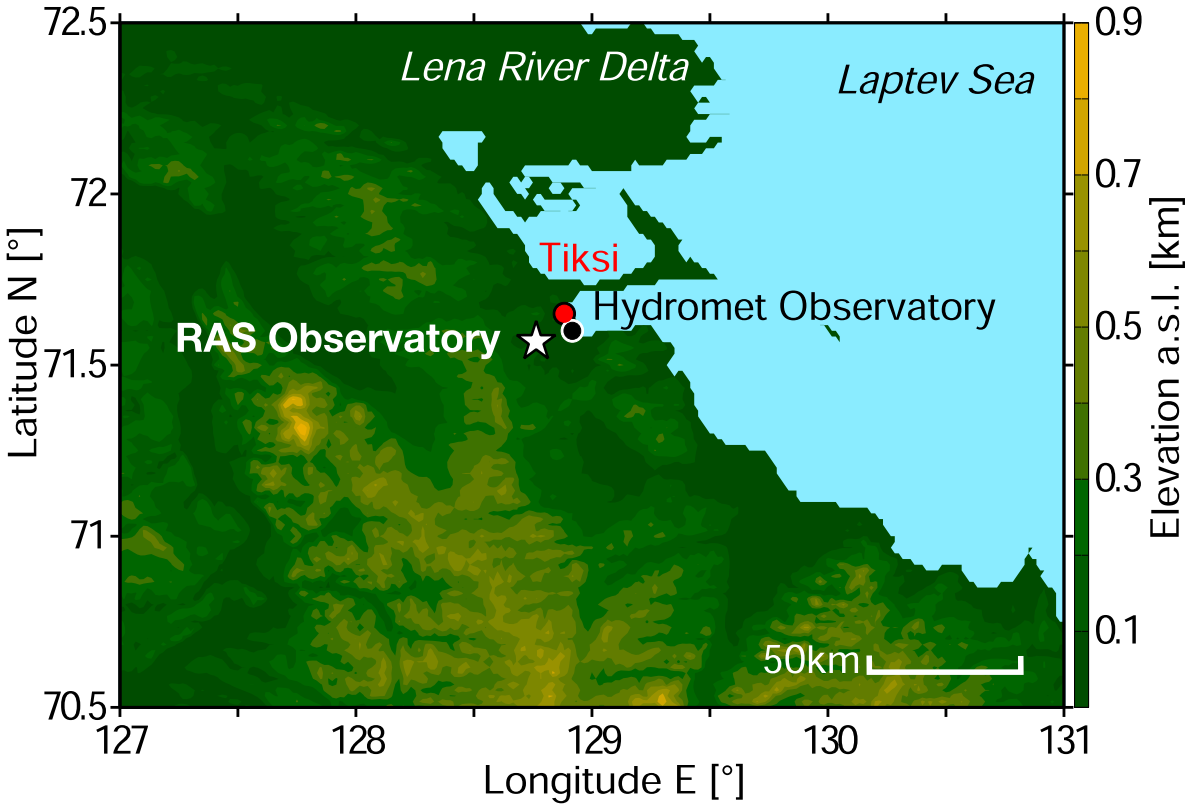

Fig. S4. The study site. Elevation map of the RAS Polar Geocosmophysical Observatory (star) and Hydromet observatory sites (black circle) in relation to Tiksi village (red circle); a.s.l., above sea level.

Table S1. Observation vs. model

Start yyyy-mm-dd	Sampling time, d	Observation				FLEXPART–ECLIPSE				
		TSP EC, ng C·m^{-3}			f_{bb}	Fossil EC, ng·m^{-3}	Biofuels EC, ng·m^{-3}	Fire EC, ng·m^{-3}	Σ EC, ng·m^{-3}	f_{bb}
2012-04-16	66.9	67.7	± 5.5		0.408	6.6	1.0	12.3	19.9	0.670
2012-06-21	63.0	37.8	± 4.3		0.731	5.1	0.6	44.8	50.5	0.899
2012-08-24	62.0	19.8	± 3.1		0.619	5.3	0.6	5.5	11.4	0.536
2012-10-25	63.0	21.2	± 3.3		0.253	17.1	1.0	0.2	18.2	0.061
2012-12-27	17.9	73.5	± 6.4		0.194	42.3	1.5	0.0	43.8	0.035
2013-02-06	21.0	302.1	± 16.2		0.080	44.9	2.2	0.0	47.1	0.046
2013-02-27	21.0	82.5	± 5.3		0.119	38.9	0.8	0.0	39.8	0.021
2013-03-20	21.0	85.8	± 5.5		0.187	4.9	0.8	0.3	6.0	0.191
2013-04-10	22.0	103.2	± 6.5		0.141	22.0	3.2	3.1	28.3	0.222
2013-05-02	21.0	63.0	± 4.4		0.239	7.4	0.9	3.0	11.3	0.340
2013-05-23	63.0	40.8	± 3.3		0.362	*	*	*	*	*
2013-07-25	84.0	8.0	± 1.5		0.600	6.0	0.4	83.8	90.2	0.934
2013-10-17	78.0	19.2	± 2.1		0.605	25.9	2.5	0.3	28.7	0.097
2014-01-02	20.1	41.0	± 3.1		0.359	32.5	1.8	0.0	34.3	0.052
2014-01-23	21.9	47.2	± 3.4		0.313	67.3	1.3	0.0	68.6	0.019
2014-02-14	21.0	43.0	± 3.2		0.300	51.6	3.0	0.2	54.8	0.058
2014-03-07	21.0	37.3	± 3.0		0.263	58.3	5.2	4.6	68.1	0.144
ALL (analog to FLEXPART)		46.7			0.304	19.8	1.4	18.1	39.3	0.398
stdev		66.7			0.200	21.2	1.3	22.6	23.8	0.316
2013-02-06 to 2014-02-14	310	55.4			0.210	23.1	1.5	23.2	47.8	0.339
stdev		87.7			0.197	20.8	0.9	27.7	26.6	0.291
2013-02-27 to 2014-03-07	310	37.4			0.290	23.5	1.5	23.2	48.3	0.339
stdev		31.6			0.180	21.6	1.0	27.7	27.0	0.290
2013-03-20 to 2014-03-28	310	34.4			0.315	24.8	1.8	23.6	50.2	0.348
stdev		30.2			0.166	23.6	1.5	27.5	28.5	0.283
2013-02-06 to 2014-02-14	373	53.3			0.227					
stdev		83.8			0.187					
2013-02-27 to 2014-03-07	373	37.9			0.302					
stdev		30.1			0.170					
2013-03-20 to 2014-03-28	373	35.4			0.323					
stdev		28.6			0.156					

TSP EC compared with FLEXPART data; stdev, standard deviation.
*No model calculations were available, i.e., observation data were excluded for the total and yearly averages.

Table S2. Stable carbon ($\delta^{13}C$) end-members for different BC sources

BC source	Liquid fossil	Coal	Gas flaring	Domestic*	Biomass†	R fossil‡
$\Delta^{14}C$, ‰	−1,000 ± 0	−1,000 ± 0	−1,000 ± 0	−265 ± 1.2	+225 ± 60	−1,000 ± 0
$\delta^{13}C$, ‰	−31.4 ± 1	−23.4 ± 1.3	−38 ± 3	−25.5 ± 36	−26.7 ± 1.8	−25.5 ± 1.3

The end-members are site-/region-specific. Applied end-members are according to Andersson et al. (28) for coal and R fossil, Mašalaitė et al. (40) for liquid fossil, and Widory (44) for gas flaring. For biomass, the $\delta^{13}C$ end-member is used according to Andersson et al. (28) and Winiger et al. (13), reflecting the photosynthesis pathway of trees. Although we applied a $\Delta^{14}C$ end-member of 225 ± 25‰ for the European Arctic (13, 31), an end-member with higher variability was used for the Russian Arctic, to account for possible differences in biota or lumbering behavior (e.g., trees older than 60 y).
*Estimated as 60% biomass, 39% coal, and 1% liquid fossil (24).
†Biomass (open fires) were used interchangeably with GFED, even though GFED captures also other events.
‡Liquid fossil fuels of regular origin, i.e., consumed in, e.g., Western Europe or China.

Table S3. Isotope analysis

Start yyyy-mm-dd	Sampling duration, d	TSP_{EC} $\Delta^{14}C$, ‰	f_{bb}	$\delta^{13}C$, ‰
2012-04-16	66.9	−500 ± 2	0.408 ± 0.026	−28.2 ± 0.2
2012-06-21	63.0	−105 ± 3	0.731 ± 0.049	−25.8 ± 0.2
2012-08-24	62.0	−242 ± 2	0.619 ± 0.046	−27.5 ± 0.2
2012-10-25	63.0	−690 ± 1	0.253 ± 0.018	−30.1 ± 0.2
2012-12-27	17.9	−762 ± 2	0.194 ± 0.029	−29.2 ± 0.2
2013-02-06	21.0	−902 ± 3	0.080 ± 0.023	−30.7 ± 0.2
2013-02-27	21.0	−855 ± 3	0.119 ± 0.028	−29.2 ± 0.2
2013-03-20	21.0	−771 ± 2	0.187 ± 0.031	−29.0 ± 0.2
2013-04-10	22.0	−827 ± 2	0.141 ± 0.031	−29.4 ± 0.2
2013-05-02	21.0	−707 ± 1	0.239 ± 0.034	−28.6 ± 0.2
2013-05-23	63.0	−556 ± 1	0.362 ± 0.038	−28.1 ± 0.2
2013-07-25	84.0	−265 ± 2	0.600 ± 0.034	−27.6 ± 0.2
2013-10-17	78.0	−259 ± 2	0.605 ± 0.015	−28.0 ± 0.2
2014-01-02	20.1	−560 ± 1	0.359 ± 0.027	−27.5 ± 0.2
2014-01-23	21.9	−616 ± 1	0.313 ± 0.023	−28.2 ± 0.2
2014-02-14	21.0	−633 ± 1	0.300 ± 0.027	−27.0 ± 0.2
2014-03-07	21.0	−677 ± 1	0.263 ± 0.028	−26.9 ± 0.2
All			0.308 ± 0.194	

Shown are isotopic data from ambient aerosol samples of the EC fraction of TSP. The uncertainties for the isotope data are based on AMS measurement errors (1 SD), and the f_{bb} uncertainty is based on MCMC calculations (including measurement and sampling uncertainties).

Table S4. Emission partitioning of the ECLIPSE EI data

Source type	Emission type
Biofuels	Residential and commercial
	Industry (combustion and processing)
	Power plants
Fossil fuels	Residential and commercial
	Residential and commercial; nonfuel activity
	Power plants, energy conversion, extraction
	Industry (combustion and processing)
	Industry (combustion and processing); nonfuel activity
	Power plants
	Power plants; nonfuel activity
	Surface transportation
	Waste
Open fires (wild fires not included via ECLIPSE)	Agricultural waste burning

All available (anthropogenic) ECLIPSE emissions were split according to their source type. Agricultural waste burning (AGW, e.g., on fields) is included in the Global Fire Emissions Database (GFED). AGW was hence excluded from the ECLIPSE emissions and implemented via GFED, to avoid double counting of AGW emissions.